Hindawi
Wireless Communications and Mobile Computing
Volume 2022, Article ID 9090494, 14 pages
https://doi.org/10.1155/2022/9090494

Research Article

Statistical Characteristics of 3D MIMO Channel Model for Vehicle-to-Vehicle Communications

Asad Saleem,[1] **Yan Xu**,[2] **Rehan Ali Khan**,[3] **Iftikhar Rasheed**,[3] **Zain Ul Abidin Jaffri**,[4] **and Md Abu Layek**[5]

[1]*Shenzhen Key Laboratory of Antennas and Propagation, The College of Electronics and Information Engineering, Shenzhen University, China 518060*
[2]*School of Opto-Electronic Engineering, Zaozhuang University, Zaozhuang, China 277160*
[3]*Department of Electrical Engineering, University of Science and Technology Bannu, Pakistan*
[4]*College of Physics and Electronic Information Engineering, Neijiang Normal University, Neijiang 641100, China*
[5]*Department of Computer Science and Engineering, Jagannath University, Dhaka, Bangladesh*

Correspondence should be addressed to Md Abu Layek; layek@cse.jnu.ac.bd

Received 20 February 2022; Revised 8 April 2022; Accepted 21 April 2022; Published 21 June 2022

Academic Editor: Khaled Maaiuf Rabie

Spatial and temporal characteristics of the propagation channel have a significant influence on multiantenna method applicability for fifth-generation- (5G-) enabled Internet of Things (IoT). In this paper, the statistical characteristics of a novel three-dimensional (3D) geometric-based stochastic model for next-generation vehicle-to-vehicle (V2V) multiple-input multiple-output (MIMO) communications under the nonisotropic scattering environment are investigated. In both line-of-sight (LoS) and non-line-of-sight (NLoS) conditions, the proposed model investigates the spatial, frequency, and temporal domain statistical distribution of multipath received signals by using the time-variant transfer function for indoor environments. The probability density function (PDF) of separation distance between the transceiver antennas, angle-of-arrival (AoA), and angle-of-departure (AoD) in the azimuth and elevation planes is derived by using closed-form expressions. For the space, time, and frequency correlation function (STF-CF), a precise analytical expression is derived based on MIMO antenna system. We further determine the effects of several model parameters on the V2V channel performance, such as tunnel width, antenna array spacing, Ricean K-factor, and moving velocity. The statistical characteristics of the MIMO channel model are validated by simulation results, confirming the flexibility and effectiveness of our proposed model in the tunnel scenario.

1. Introduction

Recently, the wireless communication technologies like multiple input multiple output (MIMO), channel coding, cooperative communication, and internet of vehicles (IoV) have played a crucial role towards the development of future communication networks [1–10]. MIMO channel, which uses hundreds or even more antennas, has received a lot of attention. It has been demonstrated that MIMO technique is capable to improve the energy and spectrum efficiency, especially in rich scattering environment. The rapid advancement of the 5G-enabled Internet-of-Things (IoT) communication systems for vehicle-to-vehicle (V2V) radio communications has acquired much more attentions [11–14]. Unlike traditional fixed to mobile cellular networks, the V2V channel uses low elevation for multiple antennas when both the transmitting and receiving antennas are conceived in motion. The radio propagation parameters between the transmitting (M_T) and receiving (M_R) antennas must be designed to facilitate the thorough investigation of V2V radio communications [15]. Therefore, the realistic propagation channel model is required which can provide a quick and easy algorithm to approximate the statistical characteristics of V2V radio channel [16, 17].

To determine the optimized performance of the V2V radio communications in tunnel environments, precise channel models are under consideration. The V2V channel models can be classified as stochastic models and

deterministic models (mostly based on the ray tracing (RT) method). Stochastic models are classified into two types: regular-shaped geometrical-based stochastic models (RS-GBSMs) [18–22] and non-regular-shaped geometrical-based stochastic models (NGBSMs). The latter, also named as parametric models, are established from channel measurements, whereas the former are constructed from the regular geometrical-shape of the scattering objects. In [18], it is proved that the line-of-sight (LoS) path between the transceiver antennas is likely to be interrupted by buildings and barriers. As a result, Ricean channels must be used to investigate V2V communication systems. In [19], a precise visual scattering model is proposed for the multibounced V2V propagation channels in crowded urban communication environment; however, they did not address the influence of moving car velocity on the V2V channel propagation characteristics. In addition, [20, 21] introduce the 3D RS-GBSMs for microcell and macrocell communication systems, respectively.

However, the majority of the RSGBSMs models are based on narrowband channel assumptions, where the rays have almost the same propagation delay [22], which is not an accurate portrayal of V2V wireless communication system. In [23], the narrowband and wideband V2V channel characteristics based on propagation delays have been investigated through the real-time measurement campaign. The wide-sense stationary uncorrelated scattering (WSSUS) assumptions are used mostly in previous channel models; however, it is only applicable for short time intervals [24]. The WSSUS means actually first- and second-order stationarity in both time and frequency domains (wide-sense stationarity in time, uncorrelated scattering in delay) and holds in successive time and frequency interval. According to the measurement campaign in [25, 26], the stationary interval, in which the WSSUS assumption is still valid for V2V environments, is substantially smaller than the observation interval. This implies that in V2V channels, the WSSUS assumptions are not being fulfilled in most of the cases. Therefore, the stochastic channel models must need to consider the channel's nonstationarity properties to compensate these shortcomings.

Similarly, in [27], the algebraic framework of the transceiver antennas in the Doppler spectrum based on moving velocity and arbitrary delays has been investigated and velocity vectors are considered to characterize the arbitrary moving direction in V2V radio communication environment. In [28], a novel 3D-GBSM model based on an ellipsoid Gaussian scattering distribution is proposed that can jointly characterize the elevation angles, azimuth angles, and distances from the transmitter (receiver) to the first (last)-bounce scatterers. The spatial consistency of the channel is supported by tracking the locations of the transmitter, receiver, and scatterers. Reference [29] proposes a statistical wideband V2V MIMO channel model based on the Unitary matrix transformation algorithm. The V2V MIMO channel model for other taps is estimated by examining the propagation delays of the first tap with a Unitary matrix transformation algorithm. In [30], a nonstationary stochastic model has been presented between the vehicle and terminal using 3D antenna arrays and random trajectories with fixed velocity consideration. In [31], the delay-based Doppler PDF for V2V radio channels is computed by using a prolate spheroidal system. In [32], the authors proposed a V2V scattering model with the assumption of randomly distributed scatterers across the semicircular shaped tunnel sidewalls. In the context of randomly moving clusters, [33] proposes a nonstationary GBSM channel model for future intelligent V2V communications. Because of the nonstationarity induced by moving clusters, the clusters' movements are described using a random walk procedure.

Also, [34] presents a regular-shaped 3D-GBSM model for V2V MIMO system for nonisotropic fading channel. However, the channel statistics of PDF, time delays, and tunnel width impact at different locations, which is critical for V2V MIMO systems, have not been investigated in the given model. Therefore, in this paper, the 3D MIMO V2V channel is modeled using the rectangular single-bounce scattering tunnel (RSBST) model, rather than the geometrical semicircular or circular tunnel propagation models. The inspiration came from the idea that both of the geometrical rectangular and semicircular tunnels are generally used in MIMO systems. As arched and rectangular tunnel environments have different propagation characteristics, therefore, we feel that our proposed model is simple and more suitable for indoor rectangular tunnel environment. To our knowledge, no investigation of radio wave propagation in rectangular tunnel from the perspective of scatterer distribution and movement of V2V MIMO systems along tunnel width has been performed.

In this paper, we investigate the new geometrical RSBST model and compute its geometrical statistics with other scattering models to examine the influence of size and cross-sectional shape of tunnels on the V2V radio channel configurations. The key contribution of this study is to analyze the effect of different RSBST model parameters on V2V channel statistics and to obtain an optimized expression for scatterer distribution. The distribution of scatterers has been derived by considering the z-axis influence on the system performance and computed the 3D STF-CF of the V2V propagation channel in LoS and NLoS propagation environments. The impacts of numerous model parameters, such as tunnel diameter, antenna array spacing, Ricean K-factor, and moving velocity, on the V2V channel statistics are investigated as well.

The remainder of this paper is arranged in the following manner. Section 2 explains the proposed RSBST system model. In Section 3, different characteristics of the 3D-GBSM channel, such as TVTF, STF-CF, and power angular spread, are derived. In Section 4, the analytical results are presented and critically analyzed. Finally, Section 5 summarizes the paper.

2. Analysis of Geometric RSBST Model

The geometrical RSBST propagation model for the V2V MIMO system inside a rectangular-shaped tunnel is described in this section. Figure 1 represents a typical propagation scenario in an L-length tunnel. As illustrated in

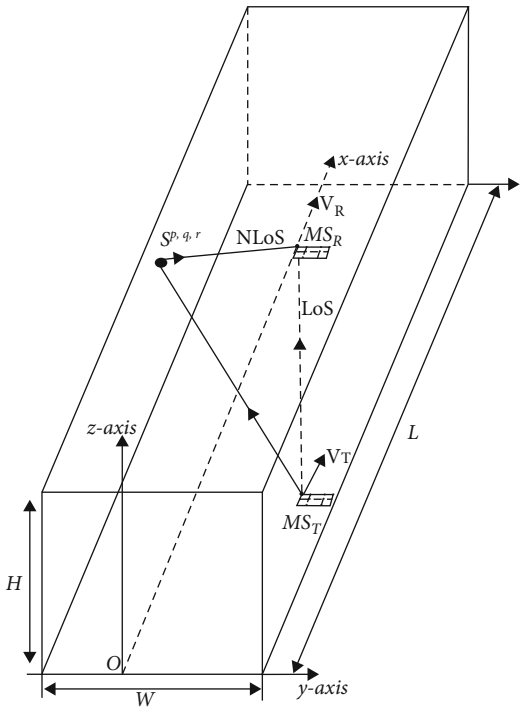

Figure 1: Propagation environments inside rectangle tunnels.

Figure 2, we assume that the scatterers are distributed randomly beside the tunnel sidewalls and ceiling. Due to cross-sectional size, shape, and geometry, the characteristics of a rectangular tunnel are substantially different from those of a circular or arch tunnel [35]. For example, in an arch tunnel, the tunnel width (W) is dependent on the tunnel radius due to semicircular geometry, whereas in a rectangular-shaped tunnel, the width (W) of the tunnel is independent from the height (H) of tunnel. As a result, when the scatterers are distributed on the tunnel ceiling and sidewalls, the z-axis affects the statistics of the V2V radio channel in a rectangular tunnel. Thus, we consider the impact of tunnels' z-axis when computing the STF-CF for next-generation V2V MIMO channel configurations in our proposed 3D RSBST model. In addition, Figure 3 shows the geometrical representation of RSBST V2V scattering model.

As illustrated in Figure 3, we employ a Cartesian coordinate approach to investigate the distribution of random scatterers S^{pqr} on the tunnel sidewalls and ceiling for $\forall m$, $1 \le p \le P$, $\forall q$, $1 \le q \le Q$, and $\forall r$, $1 \le r \le R$. On the rectangle tunnel sidewalls and ceiling, we suppose that the infinite number of scattering components (i.e., P, Q, $R \longrightarrow \infty$) is distributed randomly [36].

However, the WSSUS assumptions can be still fulfilled for V2V radio channels over the small time periods [26]. Therefore, the V2V radio channel inside the tunnel is assumed to be WSSUS in our analysis. The locations of the receiver (MS_R) and transmitter (MS_T) are defined by cartesian coordinates $(x_{R_X}, y_{R_X}, z_{R_X})$ and $(x_{T_X}, y_{T_X}, z_{T_X})$, when MS_R and MS_T are both moving in the opposite or same directions with velocity v. φ_{Rv} and φ_{Tv} determine the angle of motion for M_R and M_T antenna elements, respectively. Additionally, the MS_R and MS_T are equipped with a multiple M_R and M_T antenna elements, and the antenna element spacing is represented by δ_R and δ_T, respectively. The path length between the mth transmitting antenna A_T^m $(m = 1, 2, \cdots, M_T)$ and the scatterer S^{pq} is denoted by $d_T^{m,pq}$, whereas the distance between the nth receiving antenna A_R^n $(n = 1, 2, \cdots, N_R)$ and the scatterer S^{pq} is denoted by $d_T^{pq,n}$. Moreover, the $d_{TR}^{m,n}$ specifies the distance between the mth element of transmitting array and the nth element of receiving array in terms of LoS path. In our work, we assume single-bounce scattering (SB) approach and further analyze the scattering effects due to randomly distributed scatterers between transceiver antennas, also known as effective scattering elements. The elevation angles and orientation of the M_R (M_T) antenna array elements with respect to the xy plane can be represented by $\phi_R(\phi_T)$ and $\gamma_R(\gamma_T)$, respectively. The symbols $\beta_T^{p,q,r}$ and $\alpha_T^{p,q}$ signify the elevation angle of departure (EAoD) and azimuth angle of departure (AAoD) of the signals that are impinging on the S^{pq} scattering elements, whereas the angles $\beta_R^{p,q,r}$ and $\alpha_R^{p,q}$ represent the elevation angle of arrival (EAoA) and azimuth angle of arrival (AAoA) of the signals which are scattered from S^{pq} scattering elements, respectively. The EAoD, EAoA, AAoD, and AAoA in coordinate system (x_p, y_q) of scattering elements are given as follows:

$$\alpha_i^{p,q} = \begin{cases} f\left(x_p, y_q\right), & \text{if } y_q \ge y_i, \\ -f\left(x_p, y_q\right), & \text{if } y_q < y_i, \end{cases}$$
$$\beta_i^{p,q} = \begin{cases} g\left(x_p, y_q\right), & \text{if } z_r \ge z_i, \\ -g\left(x_p, y_q\right), & \text{if } z_r < z_i, \end{cases} \tag{1}$$

where $i = R$ or $i =$ and, the index i relates to the receiver or transmitter. The functions $f(x_p, y_q)$ and $g(x_p, y_q)$ are defined as follows:

$$f\left(x_p, y_q\right) = \cos^{-1}\left(\frac{x_p - x_i}{\sqrt{\left(x_p - x_i\right)^2 + \left(y_p - y_i\right)^2}}\right), \tag{2}$$

$$g\left(x_p, y_q\right) = \cos^{-1}\left(\frac{\sqrt{\left(x_p - x_i\right)^2 + \left(y_p - y_i\right)^2}}{\sqrt{\left(x_p - x_i\right)^2 + \left(y_p - y_i\right)^2 + \left(z_p - z_i\right)^2}}\right). \tag{3}$$

3. Statistical Characteristics of RSBST V2V Model

The reference model for the V2V MIMO channel under direct (LoS) and diffuse (NLoS) propagation conditions is presented here. The time-variant transfer function (TVTF),

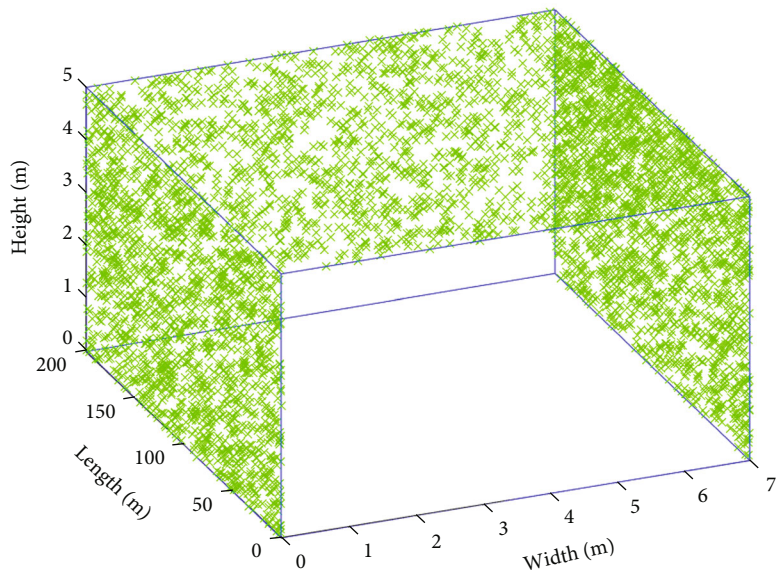

FIGURE 2: The distribution of scatterers along the sidewalls and ceiling of a tunnel when $W = 7$ m, $H = 5$ m, and length $L = 200$ m.

STF-CF, and power angular spread will be calculated from the geometrical RSBST scattering model and provided as a sum of LoS and diffuse components.

3.1. TVTF. The TVTF is denoted as $H_{nm}(t,f)$, which is the sum of LoS and diffuse components as

$$H_{nm}(t,f) = H_{nm}^{\mathrm{LoS}}(t,f) + H_{nm}^{\mathrm{diffuse}}(t,f), \tag{4}$$

where $H_{nm}^{\mathrm{LoS}}(t,f)$ and $H_{nm}^{\mathrm{diffuse}}(t,f)$ represent the TVTF of LoS and diffuse components, respectively. The $H_{nm}^{\mathrm{LoS}}(t,f)$ of LoS components is written as follows:

$$H_{nm}^{\mathrm{LoS}}(t,f) = \sqrt{\frac{k_{\mathrm{R}}^{\mathrm{LoS}}}{k_{\mathrm{R}}^{\mathrm{LoS}}+1}} e^{-j(2\pi/\lambda)d_{\mathrm{TR,LoS}}^{m,n}} e^{j2\pi\left[f^o t - \tau_{nm}^o f\right]}, \tag{5}$$

where

$$\begin{aligned} d_{\mathrm{TR,LoS}}^{m,n} = {} & d^o - (M_{\mathrm{T}} - 2m + 1)\frac{\delta_{\mathrm{T}}}{2}\cos\gamma_{\mathrm{T}}\cos\phi_{\mathrm{T}} \\ & - (M_{\mathrm{R}} - 2n + 1)\frac{\delta_{\mathrm{R}}}{2}\cos\left(\alpha_{\mathrm{T}}^o - \gamma_{\mathrm{R}}\right)\cos\phi_{\mathrm{R}}, \end{aligned} \tag{6}$$

$$d^o = \sqrt{(x_{\mathrm{R}} - x_{\mathrm{T}})^2 + (y_{\mathrm{R}} - y_{\mathrm{T}})^2 + (z_{\mathrm{R}} - z_{\mathrm{T}})^2}, \tag{7}$$

$$f^o = f_{\mathrm{T}}^o + f_{\mathrm{R}}^o, \tag{8}$$

$$f_{\mathrm{T}}^o = f_{\mathrm{T}_m}^o \cos\left(\beta_{\mathrm{T}}^o\right)\cos\left(\alpha_{\mathrm{R}}^o - \varphi_v^{\mathrm{T}}\right), \tag{9}$$

$$f_{\mathrm{R}}^o = f_{\mathrm{R}_m}\cos\left(\beta_{\mathrm{R}}^o\right)\cos\left(\alpha_{\mathrm{R}}^o - \varphi_v^{\mathrm{R}}\right). \tag{10}$$

In (8), the Doppler shifts of the LoS components generated by the movement of the M_{T} and M_{R} antennas are denoted by f_{T}^o and f_{R}^o, respectively. The angles β_{T}^o, α_{T}^o, β_{R}^o, and α_{R}^o in (9) and (10) represent the EAoD, AAoD, EAoA, and AAoA of the LoS component, respectively. The $k_{\mathrm{R}}^{\mathrm{LoS}}$ in (5) provides the Ricean K-factor, which is defined as the mean power ratio of LoS component with the diffuse components. In (5), τ_{nm}^o represents the propagation delays of LoS components and given by $\tau_{nm}^o = d_{\mathrm{TR,LoS}}^{m,n}/c_o$, where c_o is speed of light. The $H_{nm}^{\mathrm{diffuse}}(t,f)$ of diffuse components for the $A_{\mathrm{T}}^m - A_{\mathrm{R}}(n)$ transmission link can be determined as

$$\begin{aligned} H_{nm}^{\mathrm{diffuse}}(t,f) = {} & \lim_{P,Q,R\longrightarrow\infty}\left(\frac{1}{\sqrt{\left(k_{\mathrm{R}}^{\mathrm{diffuse}}+1\right)PQR}}\right)\sum_{p,q,r=1}^{P,Q,R} e^{j} \\ & \left[\theta^{p,q,r} + 2\pi\left(f_{\mathrm{T}}^{p,q,r} + f_{\mathrm{R}}^{p,q,r}\right)t - 2\pi\tau_{nm}^{p,q,r} f\right] \times e^{-j(2\pi/\lambda)\left(d_{\mathrm{T}}^{m,pq} + d_{\mathrm{R}}^{pq,n}\right)}, \end{aligned} \tag{11}$$

where

$$f_{\mathrm{T}}^{p,q,r} = f_{\mathrm{T}_m}\cos\left(\beta_{\mathrm{T}}^{p,q,r}\right)\cos\left(\alpha_{\mathrm{T}}^{p,q} - \varphi_v^{\mathrm{T}}\right), \tag{12}$$

$$f_{\mathrm{R}}^{p,q,r} = f_{\mathrm{R}_m}\cos\left(\beta_{\mathrm{R}}^{p,q,r}\right)\cos\left(\alpha_{\mathrm{R}}^{p,q} - \varphi_v^{\mathrm{R}}\right), \tag{13}$$

$$\begin{aligned} d_{\mathrm{T}}^{m,pq} = {} & \sqrt{(x_m - x_{\mathrm{T}})^2 + (y_m - y_{\mathrm{T}})^2 + (z_m - z_{\mathrm{T}})^2} \\ & - (M_{\mathrm{T}} - 2m + 1)\frac{\delta_{\mathrm{T}}}{2} \\ & \left[\cos\beta_{\mathrm{T}}^{p,q,r}\cos\phi_T \times \cos\left(\gamma_{\mathrm{T}} - \alpha_{\mathrm{T}}^{p,q}\right) + \sin\beta_{\mathrm{T}}^{p,q,r}\sin\phi_{\mathrm{T}}\right], \end{aligned} \tag{14}$$

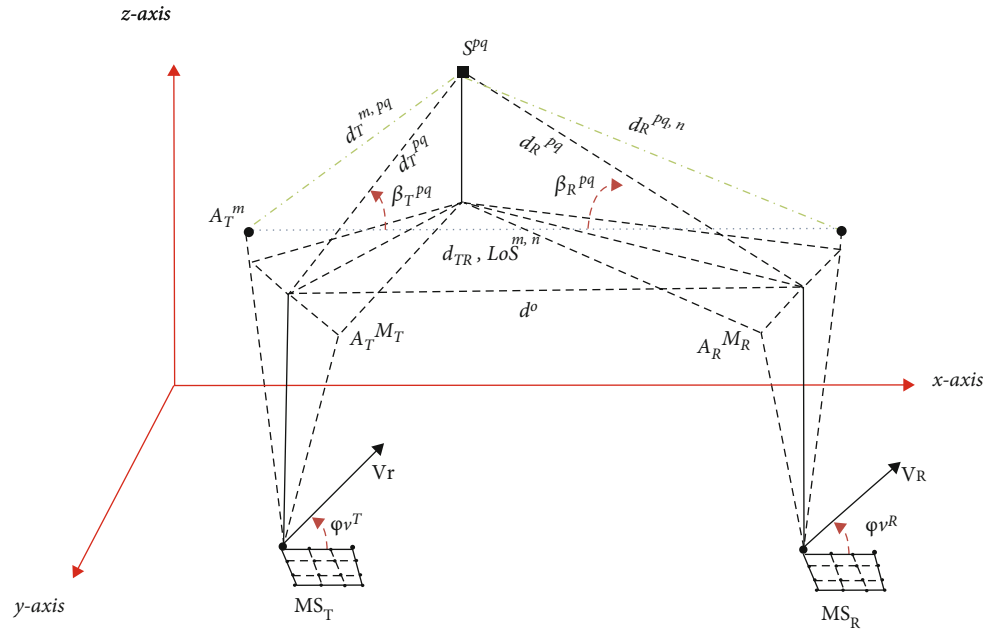

FIGURE 3: Geometrical RSBST scattering model in the presence of specular component (- · -) and LoS component (····) for $M_T \times M_R$ MIMO RSBST channel.

$$d_R^{pq,n} = \sqrt{(x_m - x_R)^2 + (y_m - y_R)^2 + (z_m - z_R)^2} - (M_R - 2n + 1)\frac{\delta_R}{2}\left[\cos\beta_R^{p,q,r}\cos\phi_R \times \cos\left(\gamma_R - \alpha_R^{p,q}\right) + \sin\beta_R^{p,q,r}\sin\phi_T\right], \tag{15}$$

where the symbols f_{T_m}, f_{R_m}, k_R^{diffuse}, and $\tau_{nm}^{p,q,r}$ represent the maximum Doppler frequency of MS_T and MS_R, Ricean K -factor, and the delays of diffuse components, respectively. In addition, $d_T^{m,pq}$ and $d_R^{pq,n}$ denote the distances between scatterer $S^{p,q,r}$ to mth transmitting antenna array A_T^m $(m = 1, 2, \cdots, M_T)$ and from the scatterer $S^{p,q,r}$ to the nth receiving antenna array components $A_R^n (m = 1, 2, \cdots, M_R)$, respectively.

3.2. STF-CF. The STF-CF is the correlation of $H_{nm}(t, f)$ and $H_{n'm'}(t + \tau, f + \upsilon)$ in (4), which can be calculated as

$$\rho_{nm,n'm'}(\delta_T, \delta_R, \tau, \nu) = E[H^*{}_{nm}(t, f) \cdot H_{n'm'}(t + \tau, f + \nu)] = \rho_{nm,n'm'}^{\text{diffuse}}(\delta_T, \delta_R, \tau, \nu) + \rho_{nm,n'm'}^{\text{LoS}}(\delta_T, \delta_R, \tau, \nu), \tag{16}$$

where $(\cdot)^*$ represents the conjugate value operator and $E(\cdot)$ denotes the expected value operator. $\rho_{nm,n'm'}^{\text{LoS}}(\delta_T, \delta_R, \tau, \nu)$ and $\rho_{nm,n'm'}^{\text{diffuse}}(\delta_T, \delta_R, \tau, \nu)$ represent the STF-CF of the LoS and the diffuse components, respectively. Thus, the STF-CF $\rho_{nm,n'm'}^{\text{LoS}}(\delta_T, \delta_R, \tau, \nu)$ can be calculated as follows:

$$\rho_{nm,n'm'}^{\text{LoS}}(\delta_T, \delta_R, \tau, \nu) = \frac{k_R^{\text{LoS}}}{k_R^{\text{LoS}} + 1} k_{mm'}^o k_{nn'}^o e^{j2\pi\left(f^o\tau + \tau'^{\,o}_{nm}\nu'\right)}, \tag{17}$$

where

$$k_{mm'}^o = e^{j2\pi(\delta_T/\lambda)\left(m - m'\right)\cos\gamma_T\cos\varphi_T}, \tag{18}$$

$$k_{nn'}^o = e^{j2\pi(\delta_R/\lambda)\left(n - n'\right)\cos\left(\alpha_R{}^o - \gamma_R\right)\cos\varphi_R}. \tag{19}$$

Moreover, $\rho_{nm,n'm'}^{\text{diffuse}}(\delta_T, \delta_R, \tau, \nu)$ can be estimated as

$$\rho_{nm,n'm'}^{\text{diffuse}}(\delta_T, \delta_R, \tau, \nu) = \lim_{P,Q,R\longrightarrow\infty}\left(\frac{1}{\sqrt{\left(k_R^{\text{diffuse}} + 1\right)PQR}}\right)\sum_{p,q,r=1}^{P,Q,R} E\left\{k_{mm'}^{p,q,r} k_{nn'}{}^{p,q,r} \times e^{j2\pi\left[f_T^{p,q,r} + \tau f_R^{p,q,r} - \tau'^{\,p,q,r}_{nm}\nu\right]}\right\}. \tag{20}$$

Note that the propagation delays $(\tau'^{\,p,q,r}_{mm})$, and the Doppler frequencies $(f_T^{p,q,r})$ are based on x_m, y_n, and z_r coordinates. Due to the infinite number of scattering elements in proposed V2V model, the random coordinates x_m, y_n, and z_r can be replaced by independent variables x, y, and z. Furthermore, the x and y are assumed to be uniformly

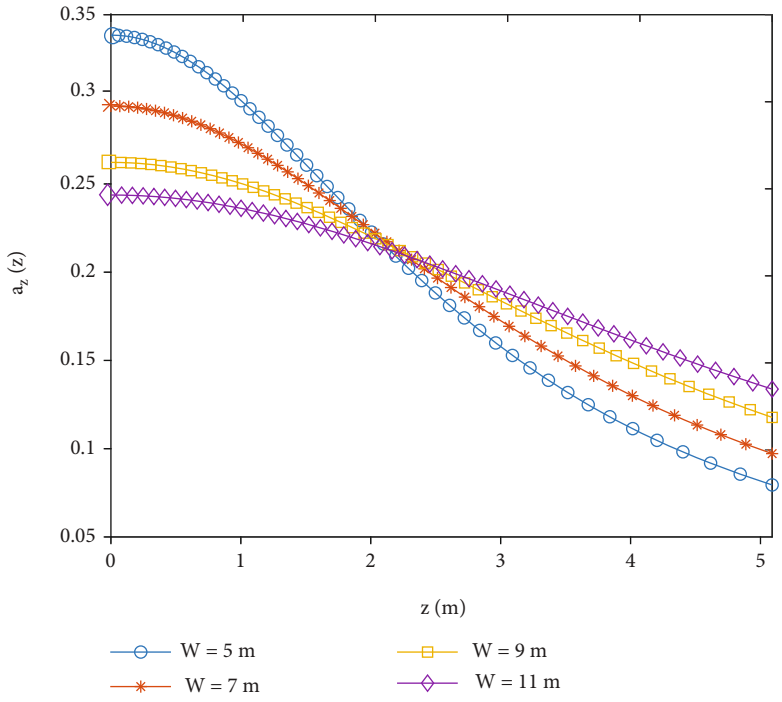

FIGURE 4: PDF $a_z(z)$ effect based on variable z and tunnel width (W).

distributed, and their PDF can be estimated as follows:

$$a_x(x) = \frac{1}{x_R - x_T}, \quad \text{if } x_R \geq x \geq x_T, \tag{21}$$

$$a_y(y) = \frac{1}{W}, \quad \text{if } \frac{W}{2} \geq x \geq -\frac{W}{2}. \tag{22}$$

The expression $z = W/2 \cdot \tan\alpha$ can be used to calculate the distribution of variable z, where z is randomly distributed in the range of $[0 \quad \tan^{-1}(2H/W)]$. By considering the transformation of given variables, the PDF of variable z can be derived as follows:

$$a_z(z) = \frac{1}{\tan^{-1}(2H/W)} \frac{2W}{W^2 + 4z^2}, \quad \text{if } H \geq z \geq 0. \tag{23}$$

The $a_z(z)$ of variable z for different widths (W) is shown in Figure 4. We can see that the $a_z(z)$ of z in (23) drops down the uniform value within the range of $z \in [0, H]$, as the width (W) of tunnel increases.

Thus, by considering PDFs of randomly distributed variables x, y, and z, the joint PDF $a_{xyz}(xyz)$ can be calculated as

$$a_{xyz}(xyz) = a_x(x) \cdot a_y(y) \cdot a_z(z),$$
$$a_{xyz}(xyz) = \frac{2}{(W^2 + 4z^2)(x_R - x_T)\tan^{-1}(2H/W)} \quad \text{if } z \in [0, H], y \in \left[\frac{W}{2}, -\frac{W}{2}\right], x \in [x_T, x_R]. \tag{24}$$

Similarly, by exploiting the joint PDF $a_{xyz}(xyz)$, the STF-CF $\rho^{\text{diffuse}}_{nm,n'm'}(\delta_T, \delta_T, \tau, \nu)$ of diffuse components in (20) can be rewritten as

$$\rho^{\text{diffuse}}_{nm,n'm'}(\delta_T, \delta_R, \tau, \nu) = A \iiint_{x_T, -W/2, 0} k_{mm'}(x, y, z) k_{nn'}(x, y, z) \times \frac{1}{W^2 + 4z^2} \times e^{j2\pi\left[f_T^{x,y,z} + \tau f_R^{x,y,z} - \tau'^{p,q,r}_{nm}\nu\right]} \tag{25}$$

where

$$A = \frac{2}{(k_R + 1)(x_R - x_T)\tan^{-1}(2H/W)}, \tag{26}$$

$$k_{mm'}(x, y, z) = e^{j2\pi(\delta_T/2)(m-m')\cos(\gamma_T - \alpha_T(x,y))\cos(\beta_T(x,y,z))\cos(\phi_T)} \times e^{j2\pi(\delta_T/2)(m-m')\sin(\beta_T(x,y,z))\sin(\phi_T)}, \tag{27}$$

$$k_{nn'}(x, y, z) = e^{j2\pi(\delta_R/2)(n-n')\cos(\gamma_R - \alpha_R(x,y))\cos(\beta_R(x,y,z))\cos(\phi_R)} \times e^{j2\pi(\delta_R/2)(n-n')\sin(\beta_R(x,y,z))\sin(\phi_R)}. \tag{28}$$

It should be noted that the propagation angles $\beta_T(x, y, z)$, $\beta_R(x, y, z)$, $\alpha_T(x, y, z)$, and $\alpha_R(x, y, z)$ in (27) and (28) are dependent on the x, y, and z coordinates of $S^{p,q,r}$.

3.3. Power Angular Spread. The power angular spread (PAS) can be configured by exploiting the Bartlett method [37]. For electromagnetic analysis, the Bartlett beamforming technique is used to estimate the angle of departure and angle of arrival in azimuth and elevation planes. The Bartlett

algorithm is predicated based on the steering vector $a(a_A^{p,q}, \beta_E^{p,q,r})$. The Bartlett beamforming algorithm is commonly known as the Fourier spectrum analyzing approach. The objective is to discover the weighting vector w that maximizes the power of the incoming signal. The receiving antenna array elements can receive the signals from different spatially distributed users. Furthermore, the received power includes both LoS and reflected (NLoS) path signals, all of which appear to be emanating from different directions and angles. The steering vector of the transmitted signals $x_1(t)$ can be estimated as

$$a\left(a_A^{p,q}, \beta_E^{p,q,r}\right) = \mathrm{vec}\left\{\begin{bmatrix} 1 \\ e^{jm} \\ e^{j2m} \\ \vdots \\ e^{j(w-1)m} \end{bmatrix} \left[1, e^{jn}, e^{j2n}, \cdots e^{j(l-1)n}\right]\right\}, \tag{29}$$

where $m = k_w d_y \cos a_A^{p,q} \cos \beta_E^{p,q,r}$, $n = k_w d_x \cos a_A^{p,q} \cos \beta_E^{p,q,r}$, λ is the wavelength, w is the width of antenna array, and l represents the length of antenna arrays, respectively. Also, d_y, d_x, $\beta_E^{p,q,r}$, and $a_A^{p,q}$ denote the antenna array spacing along the y-axis, antenna array spacing along the x-axis, elevation angle along the positive y-axis, and azimuth angle along the positive $x-$ axis. Furthermore, the signal vector of the arrays can be written as

$$y(t) = a\left(a_A^{p,q}, \beta_E^{p,q,r}\right)x_1(t) + n(t)\ , \tag{30}$$

where $n(t)$ denotes the noise power. Also, if K sources have the same time slot and frequency, the received signals can be written as follows:

$$y(t) = \sum_{k=1}^{K} a\left(a_A^{p,q}, \beta_E^{p,q,r}\right)x_k(t) + n(t). \tag{31}$$

By assuming that the received signals are coming through the azimuth direction, so the output of the array by Bartlett can be calculated as follows:

$$\max E\left\{w^H y(t) y^H(t) w\right\} = \max E\left\{x(t)|^2 \left|w^H \cdot a\left(a_A^{p,q}, \beta_E^{p,q,r}\right)\right|^2 . \sigma^2 |w|^2\right\}, \tag{32}$$

where σ^2 represents the noise power variance and $[\cdot]^H$ specifies the transpose conjugate of the given vector. The significant solution of (29) is as follows:

$$w_B = \frac{a\left(a_A^{p,q}, \beta_E^{p,q,r}\right)}{\sqrt{a\left(a_A^{p,q}, \beta_E^{p,q,r}\right)^H a\left(a_A^{p,q}, \beta_E^{p,q,r}\right)}}\ , \tag{33}$$

where $a(a_A^{p,q}, \beta_E^{p,q,r})$ denotes the normalized vector; thus, the weighting vector of the Bartlett algorithm becomes

$$w_B = a\left(a_A^{p,q}, \beta_E^{p,q,r}\right)\ . \tag{34}$$

This means that the weighting vector is the same as the incident wave spatial characteristics. The final expression for estimating the PAS is given here only. Reference [37] contains further information about the Bartlett algorithm. The PAS of $a(a_A^{p,q}, \beta_E^{p,q,r})$ can be estimated as

$$P\left(a_A^{p,q}, \beta_E^{p,q,r}\right) = \frac{a\left(a_A^{p,q}, \beta_E^{p,q,r}\right)^H R_{xx} a\left(a_A^{p,q}, \beta_E^{p,q,r}\right)}{a\left(a_A^{p,q}, \beta_E^{p,q,r}\right)^H a\left(a_A^{p,q}, \beta_E^{p,q,r}\right)}\ , \tag{35}$$

where R_{xx} is the covariance matrix of received signals, and it may be calculated as

$$R_{xx} = \frac{1}{M_{\mathrm{R}} \times M_{\mathrm{T}}} \sum_{i=1}^{I} vec[Y(i)]\mathrm{vec}[Y(i)]^H\ , \tag{36}$$

where $Y(i) \in C^{M_{\mathrm{R}} \times M_{\mathrm{T}}}$ denotes the received signals at the ith delay bin and vec$[\cdot]$ is the linear transformation operator, which sequentially turns the matrix columns into a single column vector. If the normalized vector $a(a_A^{p,q}, \beta_E^{p,q,r})$ is used, the total PAS can be stated as

$$P\left(a_A^{p,q}, \beta_E^{p,q,r}\right) = a\left(a_A^{p,q}, \beta_E^{p,q,r}\right)^H R_{xx} a\left(a_A^{p,q}, \beta_E^{p,q,r}\right)\ . \tag{37}$$

In V2V scenario, the geometric path length is usually time-variant due to the relative movement between the M S_{R} and MS_{T} antenna arrays. Compared to several existing 3D and 2D fixed-to-mobile (F2M) and V2V channel models, the proposed channel model can be utilized more efficiently in tunnel environment; for example, as the relative time is equal to zero, the proposed model tends to be wide-sense-stationary (WSS) channel, which is similar to the F2M channel [38]. However, the proposed model represents nonstationary V2V channels where the relative time is not equal to zero, as described in [39]. Moreover, the proposed 3D model can reflects a wide range of communication scenarios by modifying the geometrical model parameters, as indicated in Sections 2 and 3. For example, the proposed channel model can represent the 3D semiellipsoid channel when the relative time is set to zero, as demonstrated in [40].

4. Numerical Result Analysis

4.1. Simulation Scenario Description and Parameter Adjustment. The numerical findings obtained by assessing the STF-CF for the LoS and the NLoS propagation environments are presented in this section. Simulations are used to verify the accuracy of the proposed analytical results. To determine the optimized performance of the V2V MIMO channel, the STF-CF under different separating distances of transceivers, different moving speed, and different K -factor values are compared with similar dimensions of an indoor tunnel between Qihua road to University station in Shanghai, China. We have considered the 8×8 MIMO

(a)

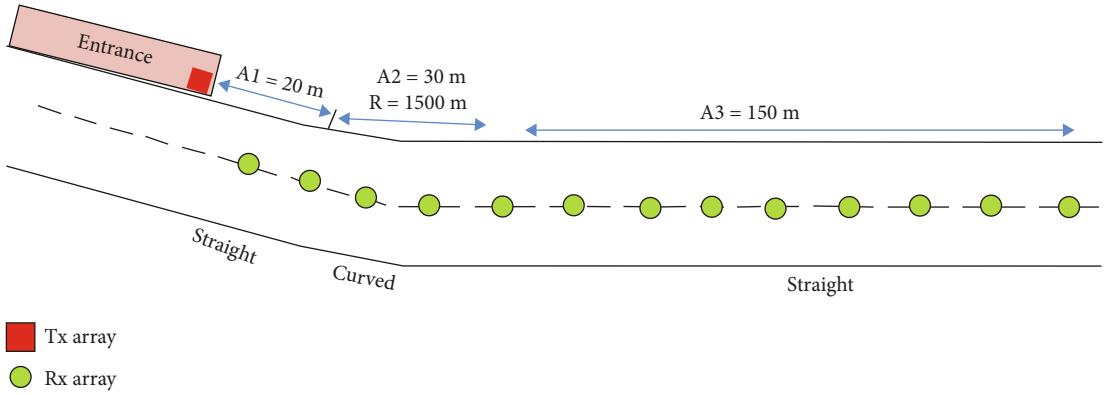

(b)

Figure 5: Simulated environment: (a) real-time tunnel view; (b) tunnel structure.

Table 1: Parameter adjustment.

Parameters	Values
Frequency	5.6 GHz
Bandwidth	160 MHz
M_T, M_R	8, 8
δ_T, δ_R	0.5 λ
Transceiver antenna array structure	Omnidirectional
ϕ_T, ϕ_R	60°
f_{T_m}, f_{R_m}	0, [120 240 360]
ϕ_T, ϕ_R	30°
γ_T, γ_R	45°
Tunnel area	200 m (length)/7 m (width)/5 m (height)
Farthest measurement distance	200 m
Number of sampling locations	101
Ricean K-factor	3, 6

system in a rectangular-shaped tunnel with a height of $L = 200$ m, a width of $W = 7$ m, and a height of $H = 5$ m using our proposed geometrical propagation model. In our simulation results, we have considered the SNR as 20 dB. Basically, the SNR is influenced by the path loss, so we have fixed it to check the influence of multipath components effect. The real-time inner view of indoor Shanghai tunnel and geometrical representation is given in Figure 5. The tunnel is divided into two sections, the first of which is a 20 m long tunnel platform or entrance with a 6.5 m high

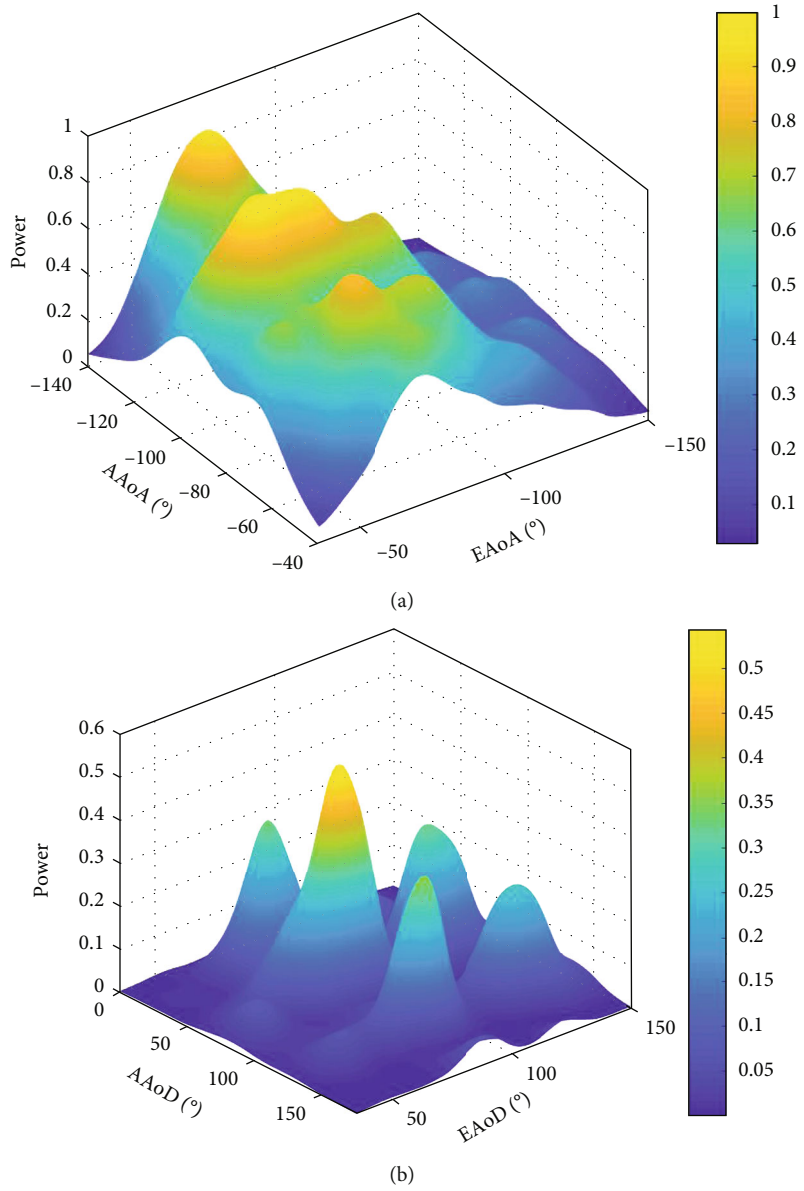

Figure 6: The azimuth and elevation polarization distribution for indoor tunnel: (a) AAAoA and EAoA; (b) AAoD and EAoD.

rectangular cross-section. A nonplatform structure with a 5.96 m high arch cross-section makes up the second section. Throughout this 200 m distance, 101 different measuring locations are taken into account, each of which is 2 m apart. The following parameters are considered to produce numerical results: $\phi_T = \phi_R = 60^\circ$, $\gamma_T = \gamma_R = 45^\circ$, $\varphi_T = \varphi_R = 30^\circ$, $(x_T = 0, y_T = 0, z_T = 3.1\,\text{m})$, $(x_R = 0, 2, \cdots, 200\,\text{m}, y_R = 3.5\,\text{m}, z_R = 2.7\,\text{m})$, and $f_{R_m}(Hz) = [120\ 240\ 360]$. The MS_T is fixed to the tunnel sidewalls at the entrance, whereas the MS_R moves along the tunnel axis. The tunnel walls are reinforced with concrete material. The propagation angles $\beta_T(x, y, z)$, $\beta_R(x, y, z)$, $\alpha_T(x, y, z)$, and $\alpha_R(x, y, z)$ are estimated according to (27) and (28). The first 50 m distance in tunnel is conceived as LoS path, where the rest of 150 m is considered as NLoS path. Table 1 also lists the additional parameters that are used to generate our simulation findings. The Monte Carlo approach [41] is used to simulate the STF-CF under various K-factors, time separations (τ), and Doppler shifts (f_{R_m}). We can use the Monte Carlo approach to multiply the iteration of the TVTF's NLoS components since the LoS components are deterministic while the NLoS components are based on a random process. The number of iterations for the Monte Carlo technique is fixed to 2×10^4 in this paper. In our simulations, we have considered the SNR as 20 dB. Basically, the SNR is influenced by the path loss, so we have fixed it to check the influence of multipath component effect. In this paper, our aim is to check the channel correlation, where the channel correlation is influenced by the SNR and channel matrix simultaneously. In our simulation results, we pay more attention to the influence of wireless channel matrix on correlation in different environments and different MS_T-MS_R distances, which requires removing

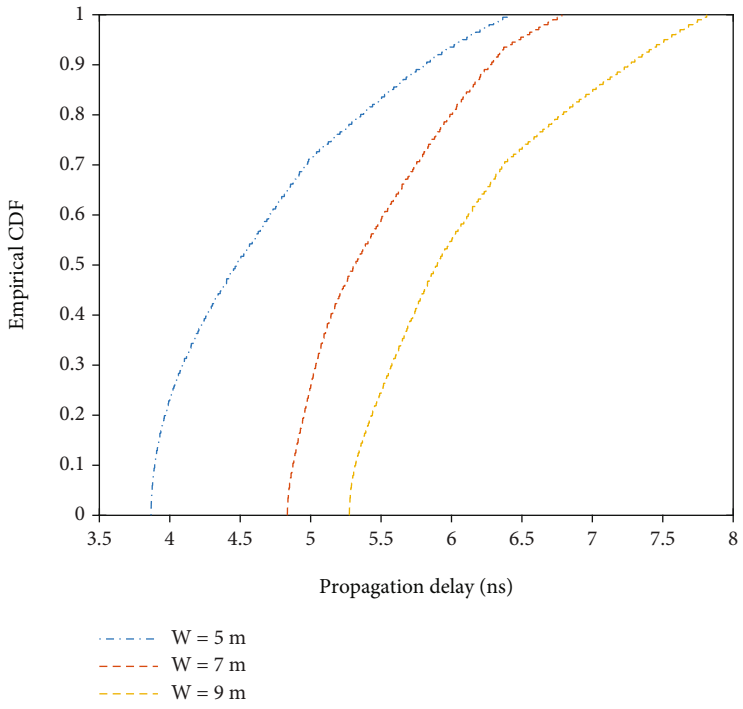

Figure 7: CDF of propagation delays with different tunnel widths (W).

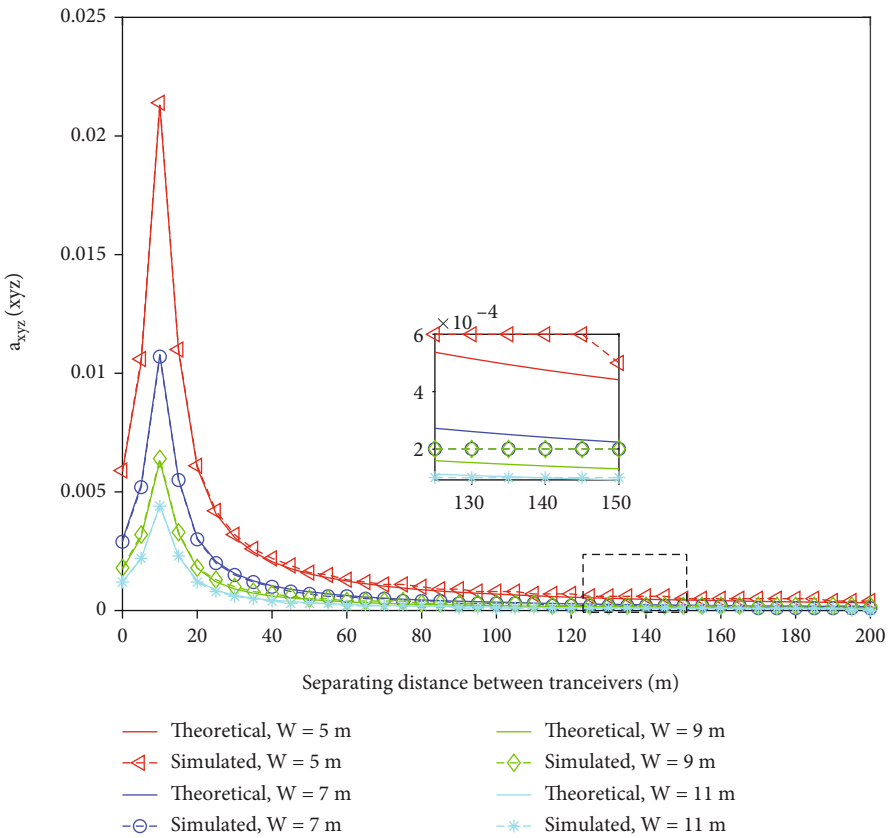

Figure 8: The joint PDF with different tunnel widths (W).

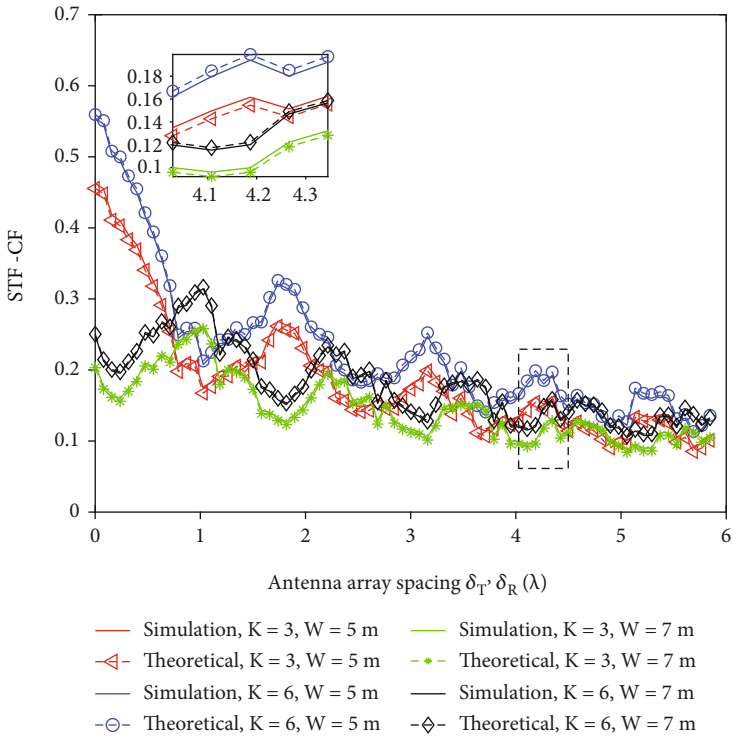

FIGURE 9: Magnitude of the STF-CFs of the RSBST model with different W and K-factor values.

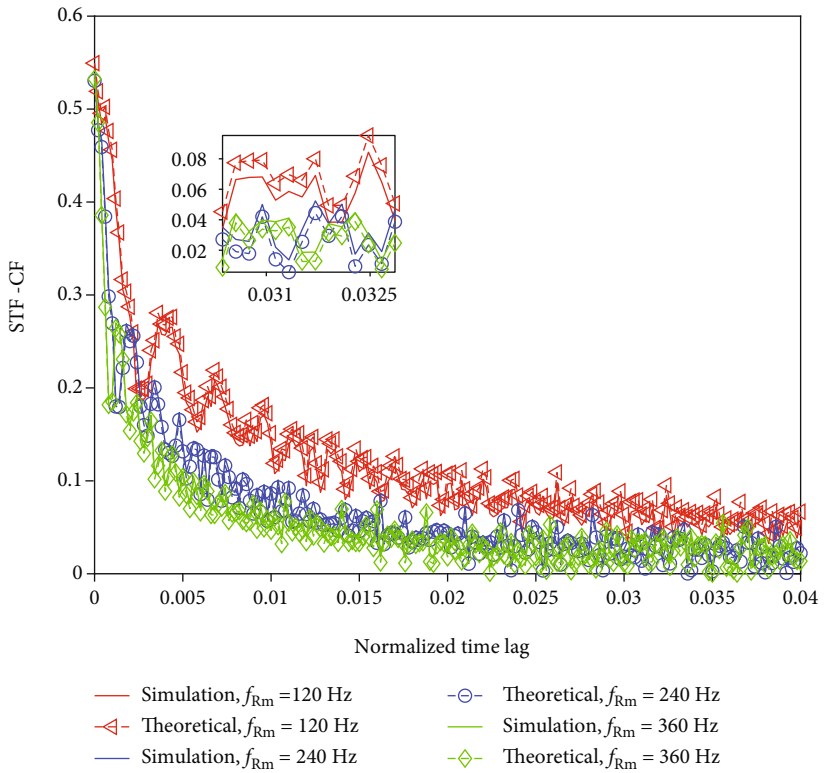

FIGURE 10: Magnitude of the STF-CFs of the RSBST model with different Doppler frequencies.

the influence of path loss and signal-to-noise ratio so that channel correlation can be compared in a fair way. After fixing the SNR, channel matrix can express the multipath effects in a proper way. In our simulations, the bandwidth is 160 MHz, which means the sampling interval of two adjacent multipath components can be as low as 6.25 ns (1/160 MHz). Because the coherent bandwidth of the channel is lower than the long-term-evolution for metro (LTE-M) signal bandwidth, we used wideband channel assumptions for the calibrations. In this paper, we have considered the reflections from the tunnel sidewalls and ceiling only for simulation results.

4.2. Angular Distribution and Propagation Delays. In Figure 6, we have shown power angular distribution by considering the elevation angle of departure (EAoD), azimuth angle of departure (AAoD), elevation angle of arrival (EAoA), and azimuth angle of arrival (AAoA) at 100 m separation distances between the transceiver antenna arrays ($x_R - x_T = 100$ m). Here, the number of scatterers is conceived as 2000 [42]. We can see that EAoA and AAoA both have negative magnitude which is because of $z_r < z_i$ and $y_q < y_i$, respectively. The power and angular spread is configured by using the Bartlett method [37]. From Figure 6, we can observe that the propagative angles reproduce two main beams at −58° of elevation and azimuth of −83° and −46° for EoA and AoA (see Figure 6(a)) and at 84° elevation and azimuths of 88° and 133° for EAoD and AAoD (see Figure 6(b)), respectively. Moreover, the propagation delays (τ) are shown in Figure 7 by using RSBST approach at 5.6 GHz operating frequency. The results represent the cumulative distribution function (CDF) of propagation delays in the presence of different tunnel widths ($W = 5$ m, 7 m, and 9 m). It can be seen that propagation delays are increased by increasing the tunnel width. A modal theory can explain this pretty well [43]. Multiple propagation modes are triggered at the shorter MS_T to MS_R distances. At a greater distance, particularly in the case of NLoS propagation, high-order model attenuation becomes critical, and only the low-order primary model is retained. As a result, the reflected environment's delay spread is relatively steady. The tunnel has a smaller path loss exponent in the given frequency band, but it still displays the waveguide effect. Furthermore, the signal's shorter wavelength (λ) increases the specular reflections, which boosts the waveguide effect in the tunnel for higher frequency transmissions. When the multipath components are obstructed by the tunnel sidewalls and ceiling, the waveguide effect is considerably decreased. Also, due to the enormous 1500 m radius of curvature (R), there are only a few path loss exponents in the NLoS region.

4.3. PDF and Correlation Function. In Figure 8, the theoretical vs. the simulation analysis of joint PDF of proposed RSBST model for different tunnel widths (W) is shown by using (24). Here, antenna array spacing is set as $\delta_T = \delta_R 0.5$ λ. It can be shown that joint PDF grows as the separation distance between the MS_T and the MS_R reduces and decreases as the width (W) of the tunnel increases. Furthermore, the simulated results are in good agreement with the theoretical values of $a_{xyz}(xyz)$, verifying the validity of the proposed model. In a multipath channel, the initial geometric path length has a significant impact on the PDF of the transceiver separation distance. It is worth noting that the MS_R and MS_T are installed in two semiellipsoid scenarios in [44], and the PDF statistics are compatible with our proposed 3D model. Due to the symmetry of the geometric radio channel model, each joint PDF $a_{xyz}(xyz)$ curve in Figure 8 is symmetric, which is also compatible with [44]. Thus, the proposed 3D MIMO model can be used to characterize the real tunnel environment.

Figure 9 presents the STT-CF for different K-factor values, when $f_{R_m} = 360$ Hz, coherence time $\tau = 1$ ns, and separating distance between transceiver arrays is $x_R - x_T = 200$ m. As shown in Figure 9, the STF-CF decreases as the tunnel width (W) or MS_T and MS_R antenna array spacing (δ_T, δ_R) increases, and the STF-CF increases as the K-factor increases. Meanwhile, the STF-CF simulation values are in good agreement with the theoretical values, indicating that the proposed model is suitable. The LoS components have a negative impact on MIMO channel performance. Figure 10 represents the STF-CF for different normalized time lag $\tau \cdot f_{R_m}$ and Doppler shift $(f_{R_m} = [120\,\text{Hz}\,(23\,\text{km/h})$, 240 Hz (46 km/h), and 360 Hz (69 km/h)]) for MS_R when $K = 3$, and distance between MS_T and MS_R is set to $x_R - x_T = 200$ m. The STF-CF of the simulation results fits very well with the theoretical results, as illustrated in Figure 10. It is worth noting that when temporal separation increases, the STF-CF decreases. In our proposed model, we have considered the LoS and diffused components which provide different STF-CF values instead of 1 under different antenna spacing and normalized time lag, as given in [45]. When the Doppler shift f_{R_m} raises, the STF-CF reduces rapidly. The moving velocity of vehicles affects the V2V channel statistics of the MIMO system, as shown in [46], and this behavior can also be shown in Figure 10.

5. Conclusions

In this paper, we have presented a novel 3D scattering model for V2V MIMO radio communications in geometrical rectangle tunnel environment. Moreover, the statistical characteristics and analytical results of the proposed model allow one to understand the real tunnel propagation environment for 5G-enabled IoT communications, as it assumes the randomly distributed scatterers along the tunnel sidewalls and ceiling. A generic analytical expression for the STF-CF has been obtained by considering the nonisotropic scattering conditions in both LoS and NLoS propagation environments. Near- and far-field effects are taken into account in this RSBST model to characterize the spherical wavefronts, resulting in AAoA, EAoA, EAoD, and AAoD statistics and PDF and STF-CF responses on the MIMO antenna arrays. It is proved that the nonstationarity, including moving direction φ_v and propagation delays, affects the MIMO channel performance. From the analytical results, we can deduce that the STT-CF is seriously affected by propagation

delay, K-factor, movement velocity of receiving antenna array, and antenna array spacing. The proposed model results are aligned very well with previous propagation models, indicating that the proposed massive MIMO channel model can be generalized.

Data Availability

The data that support the research findings are available on request. The data are not publicly available due to the privacy of research participants.

Conflicts of Interest

The authors declare that there are no conflicts of interest regarding the publication of this paper.

References

[1] W. U. Khan, X. Li, A. Ihsan, M. A. Khan, V. G. Menon, and M. Ahmed, *NOMA-enabled optimization framework for next-generation small-cell IoV networks under imperfect SIC decoding (IoTV)*, EEE Transactions on Intelligent Transportation Systems, 2021.

[2] M. Asif, W. Zhou, M. Ajmal, and N. A. Khan, "A construction of high performance quasicyclic LDPC codes: a combinatoric design approach," *Wireless Communications and Mobile Computing*, vol. 2019, 10 pages, 2019.

[3] W. U. Khan, T. N. Nguyen, F. Jameel et al., *Learning-based resource allocation for backscatter-aided vehicular networks*, IEEE Transactions on Intelligent Transportation Systems, 2021.

[4] A. Saleem, F. Zhang, M. Wang, X. Yin, and G. Zheng, "Proficiency of leaky coaxial cable-based MIMO system using radiated field distribution," *International Journal of Antenna and Propagation*, vol. 2018, 13 pages, 2018.

[5] M. Asif, W. Zhou, Q. Yu, X. Li, and N. A. Khan, "A deterministic construction for jointly designed quasicyclic LDPC coded-relay cooperation," *Wireless Communications and Mobile Computing*, vol. 2019, 12 pages, 2019.

[6] W. U. Khan, M. A. Javed, T. N. Nguyen, S. Khan, and B. M. Elhalawany, *Energy-efficient resource allocation for 6G backscatterenabled NOMA IoV networks*, IEEE Transactions on Intelligent Transportation Systems, 2021.

[7] M. Asif, W. Zhou, Q. Yu, S. Adnan, M. S. Ali, and M. S. Iqbal, *Jointly designed quasi-cyclic LDPC-coded cooperation with diversity combining at receiver*, IEEE Transactions on Intelligent Transportation Systems, 2020.

[8] A. Saleem, M. Wang, G. Zheng, and X. Yin, "Spatial characteristics of wideband channels using leaky coaxial cables in tunnel scenario," *International Journal of Antenna and Propagation*, vol. 2019, 2019.

[9] M. Asif, W. U. Khan, H. Afzal et al., "Reduced-complexity LDPC decoding for next-generation IOT networks," *Wireless Communications and Mobile Computing*, vol. 2021, 10 pages, 2021.

[10] W. U. Khan, F. Jameel, N. Kumar, R. Jäntti, and M. Guizani, "Backscatter-enabled efficient V2X communication with non-orthogonal multiple access," *IEEE Transactions on Vehicular Technology*, vol. 70, no. 2, pp. 1724–1735, 2021.

[11] M. N. Peter and M. P. Rani, "V2V communication and authentication: the internet of things vehicles(IoTV)," *Wireless Personal Communications*, vol. 120, no. 1, pp. 231–247, 2021.

[12] C. Zhao, M. Dong, K. Ota, J. Li, and J. Wu, "Edge-MapReduce-based intelligent information-centric IoV: cognitive route planning," *IEEE Access*, vol. 7, pp. 50549–50560, 2019.

[13] S. Al-Sarawi, M. Anbar, K. Alieyan, and M. Alzubaidi, "Internet of Things (IoT) communication protocols: Review," in *2017 8th International Conference on Information Technology (ICIT)*, pp. 685–690, Amman, Jordan, 2017.

[14] N. Faisal, M. Shirvanimoghaddam, Y. Li, and B. Vucetic, "Non-orthogonal HARQ for URLLC: design and analysis," *IEEE Internet of Things Journal*, vol. 8, no. 24, pp. 17596–17610, 2021.

[15] C. Zhang, K. Ota, J. Jia, and M. Dong, "Breaking the blockage for big data transmission: gigabit road communication in autonomous vehicles," *IEEE Communications Magazine*, vol. 56, no. 6, pp. 152–157, 2018.

[16] L. Bai, Z. Huang, Y. Li, and X. Cheng, "A 3D cluster-based channel model for 5G and beyond vehicle-to-vehicle massive MIMO channels," *IEEE Transactions on Vehicular Technology*, vol. 70, no. 9, pp. 8401–8414, 2021.

[17] A. Saleem, M. Wang, and G. Zheng, "Scattering of electric field from leaky coaxial cable in confined area," *International Journal of Antenna and Propagation*, vol. 2017, 9 pages, 2017.

[18] A. S. Akki and F. Haber, "A statistical model for mobile-to-mobile land communication channel," *IEEE transactions on vehicular technology*, vol. 35, no. 1, pp. 2–7, 1986.

[19] H. Jiang, Z. Zhang, J. Dang, and L. Wu, "Analysis of geometric multibounced virtual scattering channel model for dense urban street environments," *IEEE Transactions on Vehicular Technology*, vol. 66, no. 3, pp. 1903–1912, 2017.

[20] J. Bian, C. X. Wang, J. Huang et al., "A 3D wideband non-stationary multi-mobility model for vehicle-to-vehicle MIMO channels," *IEEE Access*, vol. 13, no. 7, pp. 32562–32577, 2019.

[21] H. Jiang, M. Mukherjee, J. Zhou, and J. Lloret, "Channel modeling and characteristics for 6G wireless communications," *IEEE Network*, vol. 35, no. 1, pp. 296–303, 2021.

[22] H. Jiang, Z. Zhang, L. Wu, J. Dang, and G. Gui, "A 3-D non-stationary wideband geometry-based channel model for MIMO vehicle-to-vehicle communications in tunnel environments," *IEEE Transactions on Vehicular Technology*, vol. 68, no. 7, p. 6257, 2019.

[23] I. Sen and D. W. Matolak, "Vehicle–vehicle channel models for the 5-GHz band," *IEEE Transactions on Intelligent Transportation Systems*, vol. 9, no. 2, pp. 235–245, 2008.

[24] A. Paier, T. Zemen, L. Bernado et al., "Non-WSSUS vehicular channel characterization in highway and urban scenarios at 5.2 GHz using the local scattering function," *international itg workshop on smart antennas*, pp. 9–15, 2008.

[25] C. X. Wang, A. Ghazal, B. Ai, Y. Liu, and P. Fan, "Channel measurements and models for high-speed train communication systems: a survey," *IEEE communications surveys & tutorials*, vol. 18, no. 2, pp. 974–987, 2016.

[26] J. Chebil, H. Zormati, and J. B. Taher, "Geometry-based channel modelling for vehicle-to-vehicle communication: a review," *International Journal of Antennas and Propagation, vol.*, vol. 2021, pp. 1–10, 2021.

[27] M. Walter and A. Dammann, "Relative positioning and velocity estimation using V2V delay and Doppler information," *Proceedings of the 31st International Technical Meeting of the Satellite Division of The Institute of Navigation*, 2018.

[28] B. Ji, C. X. Wang, X. Gao, X. You, and M. Zhang, "A general 3D non-stationary wireless channel model for 5G and beyond," *IEEE Transactions on Wireless Communications*, vol. 20, no. 5, 2021.

[29] J. Hao, B. Xiong, Z. Zhang et al., "Novel statistical wideband MIMO V2V channel modeling using unitary matrix transformation algorithm," *PIEEE Transactions on Wireless Communications*, vol. 20, no. 8, pp. 4947–4961, 2021.

[30] A. Naeem, B. Hua, Q. Zhu, K. Mao, and J. Bao, "A novel GBSM for non-stationary V2V channels allowing 3D velocity variations," *Sensors*, vol. 21, no. 9, 2021.

[31] M. Walter, D. Shutin, and U. W. Fiebig, "Prolate spheroidal coordinates for modeling mobile-to-mobile channels," *IEEE Antennas and Wireless Propagation Letters*, vol. 14, pp. 155–158, 2015.

[32] N. Avazov and P. Matthias, "A novel wideband MIMO car-to-car channel model based on a geometrical semi-circular tunnel scattering model," *IEEE Transactions on Vehicular Technology*, vol. 65, pp. 1070–1082, 2015.

[33] X. Baiping, Z. Zhang, J. Zhang, H. Jiang, J. Dang, and L. Wu, "Novel multi-mobility V2X channel model in the presence of randomly moving clusters," *IEEE Transactions on Wireless Communications*, vol. 20, no. 5, pp. 3180–3195, 2021.

[34] J. Huang, W. Cheng-Xiang, C. Hengtai, S. Jian, and G. Xiqi, "Multi-frequency multi-scenario millimeter wave MIMO channel measurements and modeling for B5G wireless communication systems," *IEEE Journal on Selected Areas in Communications*, vol. 38, no. 9, pp. 2010–2025, 2020.

[35] A. Hrovat, G. Kandus, and T. Javornik, "Impact of tunnel geometry and its dimensions on path loss at UHF frequency band," *Proceedings of the International Conference on Circuits, Systems, Communications & Computers (SysCon')*, pp. 253–258, 2011.

[36] J. M. Molina-Garcia-Pardo, M. Lienard, and P. Degauque, *Wireless communications in tunnel*, In Tech, Rijeka, Croatia, 2012.

[37] M. A. Sadoon, R. Abd-Alhameed, and N. J. McEwan, "The impact of the covariance matrix sampling on the angle of arrival estimation accuracy," *Inventions*, vol. 4, no. 3, pp. 43–63, 2019.

[38] P. Petrus, J. H. Reed, and T. S. Rappaport, "Geometrical-based statistical macrocell channel model for mobile environments," *IEEE Transactions on Communications*, vol. 50, no. 3, pp. 495–502, 2002.

[39] N. Avazov and M. Pätzold, "A geometric street scattering shannel model for car-to-car communication systems," in *International Conference on Advanced Technologies for Communications*, pp. 224–230, Da Nang, Vietnam, 2011.

[40] J. Chen, S. Wu, S. Liu, C. Wang, and W. Wang, "On the 3-D MIMO channel model based on regular-shaped geometry-based stochastic model," in *2015 International Symposium on Antennas and Propagation (ISAP*, Hobart, TAS, Australia, 2015.

[41] G. Li, L. Klingbeil, F. Zimmermann, S. Huang, and H. Kuhlmann, "An integrated positioning and attitude determination system for immersed tunnel elements: a simulation study," *Sensors*, vol. 20, no. 24, p. 7296, 2020.

[42] R. Zhicheng, F. Zhang, G. Zheng, A. Saleem, and K. Guan, "A 3D non-stationary channel model with moving mobile station in rectangular tunnel," *International Journal of Antennas and Propagation*, vol. 2019, Article ID 6750153, 12 pages, 2019.

[43] D. G. Dudley, M. Lienard, S. F. Mahmoud, and P. Degauque, "Wireless propagation in tunnels," *IEEE Antennas and Propagation Magazine*, vol. 49, no. 2, pp. 11–26, 2007.

[44] M. Riaz, N. M. Khan, and S. J. Nawaz, "A generalized 3-D scattering channel model for spatiotemporal statistics in mobile-to-mobile communication environment," *IEEE Transactions on Vehicular Technology*, vol. 64, no. 10, pp. 4399–4410, 2015.

[45] G. Bakhshi, R. Saadat, and K. Shahtalebi, "Modeling and simulation of MIMO mobile-to-mobile wireless fading channels," *International Journal of Antennas and Propagation*, vol. 2012, 13 pages, 2012.

[46] H. Jiang, Z. Zhang, L. Wu, and J. Dang, "Three-dimensional geometry-based UAV-MIMO channel modeling for A2G communication environments," *IEEE Communications Letters*, vol. 22, no. 7, pp. 1438–1441, 2018.